Т. 89, № 2 **ЖУРНАЛ ПРИКЛАДНОЙ СПЕКТРОСКОПИИ** МАРТ — АПРЕЛЬ 2022
V. 89, N 2 **JOURNAL OF APPLIED SPECTROSCOPY** MARCH — APRIL 2022

STRUCTURAL, OPTICAL, AND PHOTOLUMINESCENCE STUDIES OF Ti-DOPED ZnO NANOPOWDERS BY A SIMPLE SOLUTION METHOD**

M. S. Kumar [1], R. V. S. S. N. Ravikumar [2], M. C. Rao [1*]

[1] Department of Physics, Andhra Loyola College, Vijayawada, India
[2] Department of Physics, Acharya Nagarjuna University, Nagarjuna Nagar,
Guntur, India; e-mail: raomc72@gmail.com

A titanium-doped ZnO nanopowder was prepared with different wt% ratios using a simple solution technique. Structural and spectroscopic characterization was done for the prepared samples. The X-ray powder diffraction pattern showed that the prepared nanopowder was in the nanoscale range, the crystallite size of the ZnO nanopowder being 41.67 nm. By increasing the dopant concentration in the host lattice, the crystalline size was decreased to 20.84 nm. The morphological surface stated that the formatting of ZnO was marginally impacted by Ti-doping. The optical properties and identification of assimilation groups were determined by UV-Vis spectroscopy. The photoluminescence spectrum indicated that the outflow groups were in the UV and red regions. Electron paramagnetic resonance displayed a reverberation signal at g = 1.35. The distinction in the magnetization values within the range from 0.04 to 0.02 was 1.092 emu/g, demonstrating an even expansion of Ti in ZnO.

Keywords: *Ti-doped ZnO, X-ray diffraction, scanning electron microscope, photoluminescence, magnetic properties.*

СТРУКТУРНЫЕ, ОПТИЧЕСКИЕ И ФОТОЛЮМИНЕСЦЕНТНЫЕ ИССЛЕДОВАНИЯ НАНОПОРОШКОВ ZnO, ЛЕГИРОВАННЫХ ТИТАНОМ МЕТОДОМ ПРОСТОГО РАСТВОРЕНИЯ

M. S. Kumar [1], R. V. S. S. N. Ravikumar [2], M. C. Rao [1*]

УДК 535.37;620.3

[1] Колледж Андхра Лойола, Виджаявада, Индия
[2] Университет Ачарьи Нагарджуны, Нагарджуна Нагар,
Гунтур, Индия; e-mail: raomc72@gmail.com

(Поступила 31 мая 2021)

Исследованы структурные и спектроскопические свойства образцов нанопорошков ZnO, легированных различной концентрацией титана с использованием простой методики растворения. Согласно рентгенограмме, размер кристаллитов нанопорошка ZnO 41.67 нм. За счет увеличения концентрации примеси в решетке-хозяине размер кристаллитов уменьшается до 20.84 нм. Морфология поверхности указывает на то, что легирование Ti незначительно влияет на формирование ZnO. Методом УФ-видимой спектроскопии определены оптические свойства образцов и проведена идентификация структурных групп. Спектр фотолюминесценции указывает на то, что группы люминесцируют в УФ и красной областях. В спектре ЭПР наблюдается сигнал реверберации при g = 1.35. Различие в значениях намагниченности в диапазоне от 0.04 до 0.02 составляет 1.092 emu/g, что свидетельствует о равномерном внедрении Ti в ZnO.

Ключевые слова: *ZnO, легированный Ti; рентгеновская дифракция; сканирующий электронный микроскоп; фотолюминесценция; магнитные свойства.*

[**] Full text is published in JAS V. 89, No. 2 (http://springer.com/journal/10812) and in electronic version of ZhPS V. 89, No. 2 (http://www.elibrary.ru/title_about.asp?id=7318; sales@elibrary.ru).

Introduction. One of the promising directions of studies is developing new materials. Among all II–VI compounds, zinc oxide (ZnO) has attracted much attention. ZnO shows unique physical and chemical properties. It possesses a direct bandgap (3.3 eV) and binding energy (60 eV) at room temperature. Moreover, it is cost-effective, nontoxic, and chemically stable [1]. ZnO shows high electrical conductivity when suitably doped. Its transparency is noticeable owing to its energy bandgap. For this reason, ZnO-based materials are widely used in different fields, including LEDs, solar cells, etc. [2, 3]. Meanwhile, doping is the best method of enhancing the properties of ZnO [4, 5].

Titanium-doped ZnO nanoparticles (NPs) are effective for optoelectronic applications. When compared with Zn, Ti has a small ionic size. The valency of the electrons for Ti is 4, whereas for Zn it is 2, which implies the possibility of doping [6], and, as a consequence, improvement of the ZnO properties [7–9]. Various experimental techniques are used for the preparation of Ti-doped ZnO nanostructures, such as chemical vapor deposition, pulsed laser deposition, radio frequency sputtering, etc. [10]. Yet, their application is expensive. For the creation of nanostructures, films, and nanopowders, the applied technique must be characterized by minimal effort, a simple procedure, and realization at room temperature [11].

As a Ti source, TiO_2 is often utilized owing to its advantages, namely, innocuousness, a wide bandgap, and chemical stability [12, 13]. In the present investigation, Ti-doped ZnO nanopowder samples at different ratios were prepared using a cost-effective and simple solution technique. The performance of the Ti doping of ZnO was examined with regard to the structural, morphological, optical, and magnetic properties.

Experimental. *Preparation of Ti-doped ZnO nanopowders.* Zinc nitrate ($Zn(NO_3)_2$), titanium dioxide (TiO_2), sodium hydroxide (NaOH), methanol (CH_3OH) from Sigma Aldrich (Bangalore, India) were used in the present investigation. The ZnO solution was prepared by dissolving an appropriate amount of $Zn(NO_3)_2$ in the presence of NaOH and CH_3OH at room temperature. A solution (20 ml) containing 0.1 M $Zn(NO_3)_2$ in CH_3OH was added dropwise to 100 ml of 0.1 M NaOH and then stirred for 30 min. Distilled water was added to the obtained solution at a ratio of 0.04, and the solution was stirred continuously for up to 30 min. The obtained solution was kept under refrigeration for 2 h for centrifugation. Later, the obtained precipitate was washed several times with distilled water and then dried at room temperature for more than 24 h, and was finally calcinated at 450 and 650°C for 2h by heating at a rate of 15°C per min [14].

Characterization. The powder X-ray diffraction (XRD) pattern of the sample was recorded on a Bruker X-ray diffractometer using CuK_α as a radiation source at a scan rate of 20 per min. The surface morphology of the prepared powder was characterized by a Carl Zeiss Neon 40 Crossbeam (Oberkochen, Germany). The energy dispersive X-ray analysis was also recorded using a Carl Zeiss Neon 40 Crossbeam. The Fourier transform infrared (FTIR) spectra of the powder samples were recorded using an ALPHA FT-IR Spectrophotometer. The optical absorption spectrum was recorded on a Czerny-Turner mounting UV-Vis Spectrophotometer in the wavelength region 200–800 nm. Photoluminescence studies of the synthesized powder were carried out with a 450W Light Xenon Source on a Jobin Yvon Fluorimeter-FL3-11 Spectro-fluorometer. The electronic *g*-factor was recorded on an ESR spectrometer (model-105). The magnetic properties of the prepared samples were measured on a Quantum Design MPMS 5XL magnetometer.

Results and discussion. *XRD analysis.* The XRD pattern of pure Ti-doped ZnO nanpowder is shown in Fig. 1. Figure 1 shows that an exceptional peak appeared at (002), indicating a hexagonal wurtzite-type structure in concurrence with JCPDS card number 01-080-0074 [15]. Based on the Ti doping percentage in ZnO, different peaks were observed in the samples. It is seen that the (002) peak of the Ti doped ZnO sample showed a wider peak than for the case of the ZnO sample. While increasing the dopant percentage, the peak intensity gradually increased. This indicates good improvement in the samples [16, 17]. From Figure 1, it is clearly observed that additional peaks appeared at (1 0 0), (1 0 1) lower from the main (002) peak at $2\theta = 36.30$, 36.48, 36.43, and 36.43°. This demonstrates the conjunction of grains. The peaks are formed by doping with different concentrations of TiO_2 in the host lattice.

The crystallite size D, the full width at half maximum (FWHM) of the prepared samples, was calculated using the Debye–Scherrer formula. The normal crystallite measurement was computed using the following equation,

$$D = k\lambda/(\beta\cos\theta), \tag{1}$$

where k is a steady equivalent to 0–9, the X-ray beam wavelength ($\lambda = 0$–15406 nm), β the FWHM, and θ the half diffraction edge.

As a result of the calculations, the crystallite size of the ZnO nanopowder was found to be 41.67 nm, and by increasing the dopant percentage up to 0.5% in the host lattice, the crystallite size of the samples was

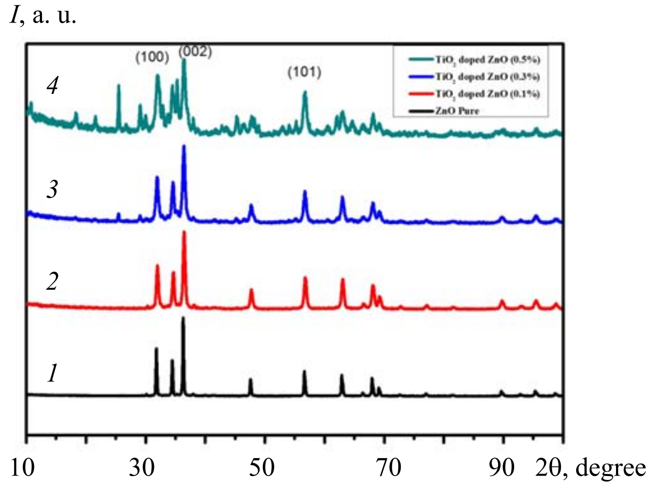

Fig. 1. XRD pattern of (1) pure ZnO, Ti-doped ZnO for (2) 0.1, (3) 0.3, and (4) 0.5%.

decreased to 20.84 nm. The FWHM changed from 0.4015 to 0.2043. The XRD pattern shows that the intensity pattern of the Ti-doped ZnO samples is similar to the undoped ZnO pattern, but a few peaks are observed with low intensity. The decrement in the FWHM demonstrates upgrading of the translucent quality [18, 19]. As observed, the normal distance of NPs is diminished and this adjusts the morphology of the prepared samples. Further, the Ti-doped ZnO is hydrothermally arranged; this outcome is disclosed owing to the expansion in the nucleation development in the grain sizes [20–23]. The lattice constant is also slightly increased after doping from 0.62475 nm for the undoped (pure) ZnO to 0.63532 and 0.63825 nm for the Ti-doped ZnO (0.5%). In addition, the pure film has a strain of −0.328%, whereas the doped samples (0.1, 0.3, and 0.5%) have a strain of −0.326, −0.311, and −0.304%, respectively. All samples have a negative strain value, which indicates the compressive strain. The undoped sample shows a compressive strain of (−0.304%). This refers to reducing the lattice constant owing to the presence of vacancies, including oxygen and zinc vacancies. It can be suggested that the incorporation of Ti into the ZnO lattice structure could enhance the growth rate of ZnO. This happens because the (002) direction has the lowest surface free energy and the Zn and O ions try to arrange into this direction. This means that the Zn and O ions are arranged in the axial direction, which is (002) more than (100) in the lateral direction. Accordingly, the average diameter of cluster particles is reduced, and the morphology of the nanopowder is altered. In our examination, the grain size decreases simultaneously. It shows that Ti could improve the smoothness of the course of action of the Zn and O particles in the appropriate locales into the grid structure, and the Ti-doped samples were methodically controlled for a good-quality nanostructure [24].

W–H analysis. Figure 2 shows a straight plot of β cos θ versus 4sinθ of the prepared samples, from which we can see that the W–H plot yields a superior coefficient relationship of the prepared samples. The *Y*-Intercept for the prepared sample is found to be at 0.0031, 0.0051, 0.0067, and 0.0066, and the particle size of the sample for pure ZnO is found to be 41.67 nm, whereas TiO_2 doped in ZnO (0.1, 0.3, and 0.5%) are found to be 38.57, 29.21, and 20.84 nm. The particle size of the samples from the plot clearly describes the decrement in the size on increasing the TiO_2 percentage [25, 26]. It is found that the grain size of the Ti-doped ZnO samples decreases with an expansion in the Ti content. This is presumably due to the Ti ions lessening the crystallinity of the ZnO.

SEM and EDX analysis. The morphological surface and energy dispersive X-ray spectroscopy (EDS) of ZnO and the Ti-doped ZnO nanopowder at different concentrations (0.1, 0.3, and 0.5%) are shown in Fig. 3a–d. It is apparent that all the prepared samples have high-caliber and thick clusters of particles. It is well known that the morphological surface of the orchestrated ZnO is marginally impacted by Ti-doping. The clusters of the nanopowder size are found to be at 41 to 20 nm for the prepared samples. The prepared samples show less consistency than pure ZnO. This might be due to the joining of Ti inside the ZnO host lattice [27, 28]. The EDS spectra uncover the presence of Zn, O, and Ti (for the doped samples). The peaks consequently show the substance of Ti increments with doping. This confirms the immaculateness of the prepared samples.

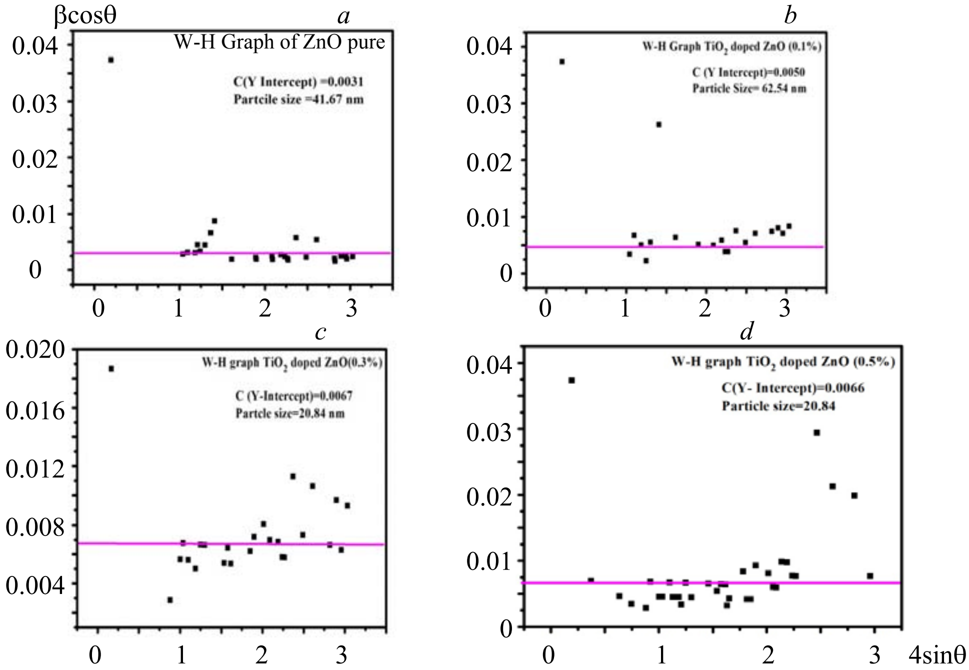

Fig. 2. Williamson–Hall analysis of (a) pure ZnO, Ti-doped ZnO for (b) 0.1, (c) 0.3, and (d) 0.5%.

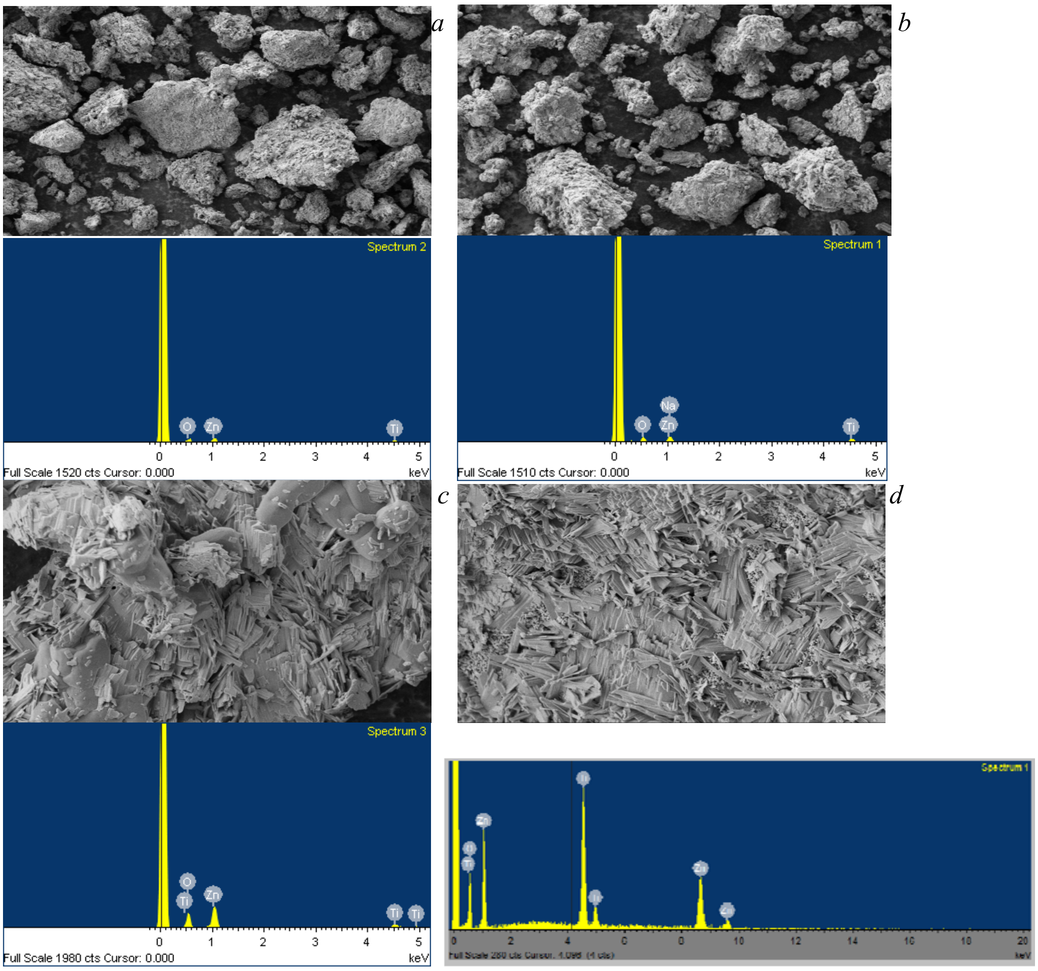

Fig. 3. Scanning electron microscopy and energy dispersive X-ray images of (a) pure ZnO, Ti-doped ZnO for (b) 0.1, (c) 0.3, and (d) 0.5%.

XPS studies. The surface formation and chemical compounds can be easily identified by the X-ray photoelectron spectroscopy (XPS) range, as per the described binding energies of the various components on material surfaces. Figure 4 demonstrates that the accompanying components are present: Zn, O, and extrinsic C. No other substances were added to the prepared sample. The XPS spectra of the Zn-2*p* center level of certain NPs are seen in Fig. 4. The NPs show a doublet at around 1.89 and 3.67 eV, compared with the Zn-$2p^{3/2}$ and $2p^{1/2}$ center levels. The main spectra are ascribed to Zn^{2+} particles in the oxygen-insufficient ZnO grid [29].

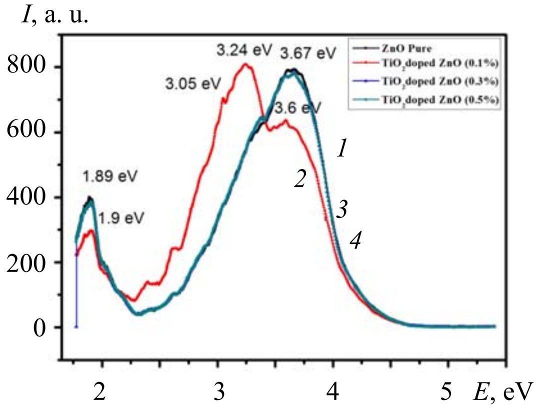

Fig. 4. XPS spectra of (1) pure ZnO, Ti-doped ZnO for (2) 0.1, (3) 0.3, and (4) 0.5%.

Additionally, all of the Zn-$2p^{3/2}$ XPS tops are sharp. Subsequently, it may be affirmed that the Zn component exists essentially as Zn^{2+}. An asymmetric peak was seen in the 3.67 district related to the contributions between the two compounds, i.e., Ti with ZnO. These two peaks are ascribed to the O_2 in the ordinary wurtzite structure of the ZnO powder and O_2^- in the oxygen-insufficient areas inside the ZnO [30]. The last segment could be credited to the presence of mostly attributed ZnO. The FWHM values might be broad owing to the amorphous nature of this material. It is because of the molecular size that the boundary peaks were not found in our NPs.

FTIR studies. FTIR is a nondestructive technique for exploring the chemical bonding presence in the samples. Figure 5 shows the FTIR range of the Ti-doped ZnO nanopowder, which was estimated within the wavenumber range 500–4000 cm^{-1}. The narrow band at 500–540 cm^{-1} was ascribed to the O–H extending mode. The C–H was due to the peak situated for the wavenumbers 1747, 2334 cm^{-1}, and the peak at 1492 cm^{-1} was because of the C–O bunch. The small peak appeared at 1236 cm^{-1} due to the C=H bond [31]. The leftover peaks at 786, 780 cm^{-1} was due to the Zn–O bond. Some of the emerging hump-like structures are shown around 525 cm^{-1}, indicating a Ti–O bond. This outcome confirms the effective doping of Ti inside the ZnO grid structure [32, 33].

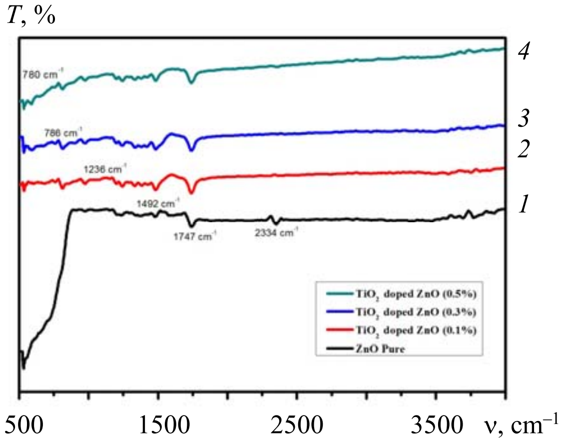

Fig. 5. FTIR spectra of (1) pure ZnO, Ti-doped ZnO for (2) 0.1, (3) 0.3, and (4) 0.5%.

Optical absorption studies. The optical absorption of the prepared samples was calculated within the wavelength range 200–800 nm for the identification of electronic transitions (Fig. 6). This range uncovers that the ZnO nanopowder has low absorbance in the visible region. From the figure, it is observed that the absorbance peak decreased. This might be due to the abatement in the hydroxide accumulation and the subsequent tempering along the grain limits [34]. From the absorption peak, it was noticed that the excitonic peak appeared at 300–373 nm related to the red region of the strain effect. The hypothesis of optical investigation gives the connection between the adsorption coefficient (α) and the photon energy ($h\nu$) for direct bandgap energy as:

$$\alpha h\nu = A(h\nu - E_g)n, \tag{2}$$

where $h\nu$ is the photon energy, E_g the bandgap, and A a constant.

Direct bandgap energy can be calculated by plotting a linear curve to the intercept axis, and it is observed that the decrement in the energy bandgap value is found to be at 3.21 to 3.15 eV. For the pure ZnO sample the bandgap is higher (3.21 eV), which could be because of the presence of ZnO, possibly in an amorphous structure [35]. Upon doping the TiO_2 percentage compositions in the samples, the energy bandgap decreases up to 3.15 eV. The dopant samples display a solid red shift in their optical spectra because of the restriction of charges in individual nanocrystals [36].

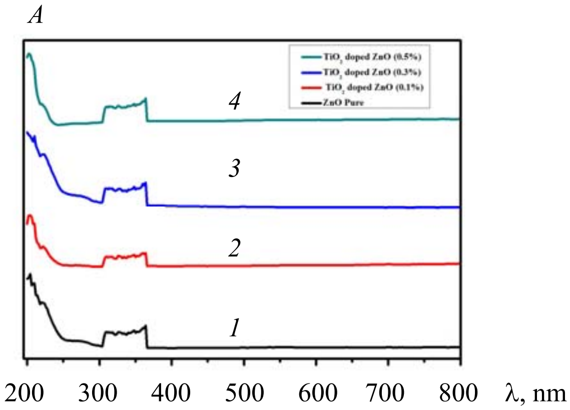

Fig. 6. Optical absorption spectra of (1) pure ZnO, Ti-doped ZnO for (2) 0.1, (3) 0.3, and (4) 0.5%.

Photoluminescence studies. The photoluminescence studies of the prepared samples measured at room temperature are shown in Fig. 7. The luminescence of free excitons in ZnO is found to be 365.5 nm and for the other prepared samples, the peaks are found to be at 365.5 and 370 nm. All the prepared samples showed two excitation peaks at 365.5 and 700 nm. The first peak is related to the recombination of free excitons. The intensity of the peak radically increases by increasing the doping percentage in the host grid as a result of the upgraded crystallinity as seen by XRD examination. The other peak, which is observed at 700 nm, related

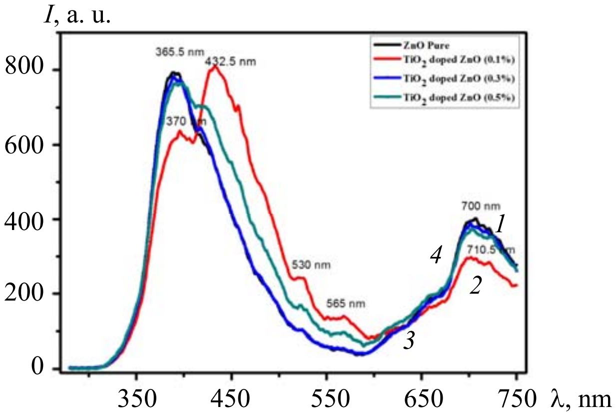

Fig. 7. PL spectra of (1) pure ZnO, Ti-doped ZnO for (2) 0.1, (3) 0.3, and (4) 0.5%.

to the point defects within the interstitial and energy bandgap, called deep level emission (DLE) [37]. After the Ti doping, the DLE improvement was noticed. However, for these TiO_2 (0.1%) samples, the peak intensity range varied with all the other compositions. This disturbance may have been formed because of the increment in the Ti^{4+} that involved Zn^{2+} in the band level [38, 39]. Additionally, small peaks situated around 432.5, 565, and 710 nm can be detected and compared with a red discharge [40]. This peak is accounted for owing to the cross-section issue along the development of NPs.

EPR studies. We examined the electron paramagnetic resonance (EPR) spectra of the titanium doped ZnO to dissect the underlying imperfections of the prepared samples. The EPR signal of the Ti-doped zinc oxide is photosensitive at low temperatures, whereas its position and amplitude depend up on the crystal orientation with respect to the field. The photo-excitation band shows up distinctively and it may be related to the deep donor of the photo-ionization. It is more reliable and even compared with the optical absorption and the bandgap energy, which turned out to be equal to 3.15 eV. In various cases, we noticed the presence of an isotopic EPR signal and the presence of a photosensitive EPR sign of '*g*' estimations, which are found to be 1.3, 1.35, 0.84, and 1.35 individually. The main sign at the g estimation of 1.35 is most likely due to the presence of the Ti^{4+} particle in the samples. From the obtained data, it is noticed that the other doping samples have the same intensity originating from the interaction of the ZnO crystal phase. In these frameworks, the inter-central red luminescence was found owing to the photo-excitation of electrons inside the restrictions of the central *d*-configuration. An EPR signal in the similar manner is recorded in zinc-oxide pottery, where it is credited to the $2S_{1/2}$ province of Ti^{4+} particles. The simultaneous application of the photo-EPR and luminescence methods is extremely promising for studying the role of point defects in thermo- and photo-stimulated electron-hole processes in crystals. As a result of the investigations, the energy position, microstructure influence, and optical and electro-physical properties of zinc oxide are found [41].

Figure 8 shows a plot of the EPR spectra from which we can see that there are ESR signals at 230 and 350 Gauss, compared with the g estimations of 1.3, 1.35, 0.84, and 1.35 individually. The main sign at the *g* estimation of 1.35 is most likely due to the presence of the Ti^{4+} particle in the samples. However, the second sign at the g estimation of 0.84 is presumably due to the presence of an oxygen opportunity in the ZnO cross section [41, 42]. This obviously demonstrates that several nano Ti^{4+} ions are immersed into the ZnO grid. Consequently, the synchronous utilization of the photo EPR and glow strategies is very encouraging for considering these studies.

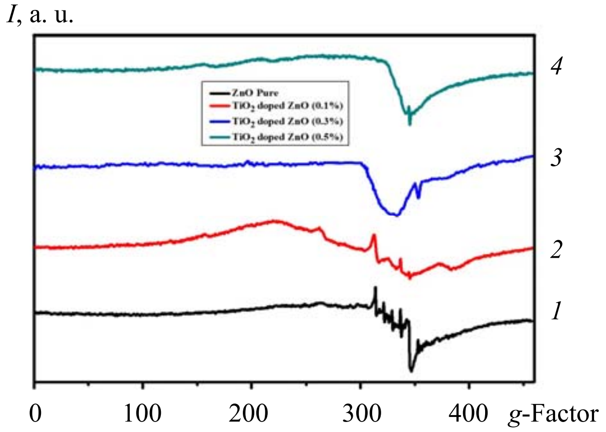

Fig. 8. EPR spectra of (1) pure ZnO, Ti-doped ZnO for (2) 0.1, (3) 0.3, and (4) 0.5%.

Magnetic properties. The magnetization versus the magnetic field curves measured at room temperature is shown in Fig. 9. From Fig. 9, it is also observed that the immersion magnetization increases with the expansion of Ti ions. The distinction in the magnetization values within the range from 0.04 to 0.02 is 1.092 emu/g, which demonstrates an even expansion of Ti in the ZnO. The observed magnetic behavior in the sample is due to the consideration of Ti^{4+} ions in the grid locales of Zn^{4+}. The imperfections initiated by Ti ions are accepted to assume the significant job of ferromagnetism in ZnO semiconductors [43]. The Ti-doped ZnO structure will give remarkable results for shaping deformities, which can be viewed as extra charge transporters. Therefore, the ferromagnetism that appeared in Ti-doped ZnO is expected in Ti^{4+} ions doped in Zn^{2+}.

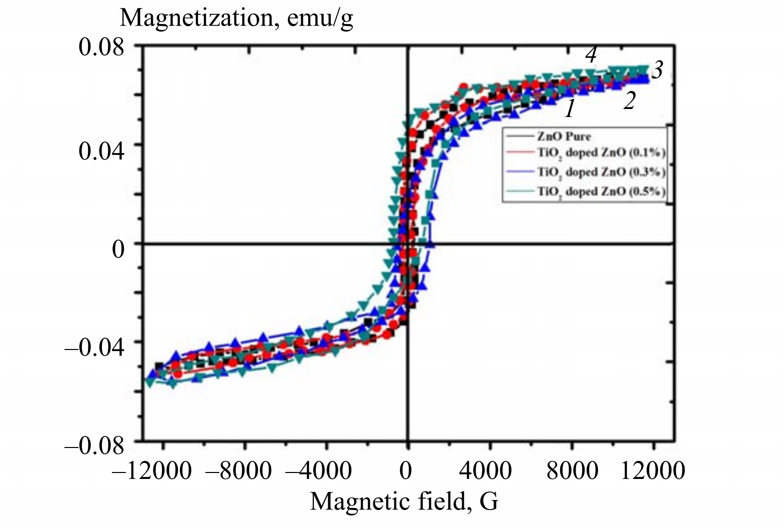

Fig. 9. Magnetization versus the magnetic field studies of (1) pure ZnO, Ti-doped ZnO for (2) 0.1, (3) 0.3, and (4) 0.5%.

Conclusions. A titanium-doped ZnO nanopowder was prepared by a simple solution technique. From the XRD pattern, it is seen that the prepared nanopowder was within the nanoscale range, and it is affirmed that the crystalline size in the samples seemed to have decreased down to 20.84 nm. It is also observed that an exceptional peak appeared at (002), indicating a hexagonal wurtzite-type structure. The FWHM ranged from 0.4015 to 0.2043. The particle size of the samples clearly describes the decrement in the size upon increasing the Ti percentage. XPS reveals that the prepared sample shows a doublet at around 1.89 and 3.67 eV compared with the Zn-2$p^{3/2}$ and 2$p^{1/2}$ center levels. The main peak is ascribed to Zn^{2+} particles in the oxygen-insufficient ZnO grid. The atomic vibrations of the prepared samples are distinguished by FTIR. The narrow band at 500–540 cm^{-1} is ascribed to the O–H extending mode. Photoluminescence studies contemplates indicate that outflow groups are in the UV and red region. The red luminescence is due to the photoexcitation of electrons inside the restrictions of the central *d*-configuration. The EPR range displays a trademark Ti^{4+} ions reverberation signal at $g = 1.35$. The immersion magnetization increases with the expansion of Ti ions. The distinction in the magnetization values within the range from 0.04 to 0.02 is 1.092 emu/g, demonstrating an even expansion of Ti in the ZnO. The outcome of the results reveals that the prepared samples are acceptable for developing solar cells, display devices, and opto-electronic gadget applications.

REFERENCES

1. S. A. Bidier, M. R. Hashim, *IEEE 6th Int. Conf. on Photonics* (2016).
2. S. A. Bidier, M. R. Hashim, Ahmad M. Al-Diabat, M. Bououdina, *Phys. E*, **88**, 169–171 (2017).
3. R. K. Chava, M. Kang, *J. Alloys Compd.*, **692**, 67–76 (2017).
4. Cheng-Liang Hsu, Yi-Dian Gao, You-Syuan Chen, Ting-Jen Hsueh, *Sens. Act. B*, **192**, 550–557 (2014).
5. R. Sridhar, C. Manoharan, S. Ramalingam, S. Dhanapandian, M. Bououdina, *Spectrochim. Acta A*, **120**, 297–303 (2014).
6. S. A. Bidier, M. R. Hashim, M. Bououdina. *J. Mater. Sci: Mater. Electron.*, **28**, 11178–11185 (2017).
7. Zhihua Yong, Tao Liu, Tomoya Uruga, Hajime Tanida, Dongchen Qi, Andrivo Rusydi, Andrew T. S. Wee, *Mater.*, **3**, No. 6, 3642–3653 (2010).
8. Liang-Wen Ji, Shi-Ming Peng, Jun-Sheng Wu, Wei-Shun Shih, Cheng-Zhi Wu, I. Tseng Tang, *J. Phys. Chem. Solids*, **70**, No. 10, 1359–1362 (2009).
9. R. Nandi, S. S. Major, *Appl. Surf. Sci.*, **399**, 305–312 (2017).
10. W. Yu, T. Liu, S. Cao, C. Wang, C. Chen, *J. Solid State Chem.*, **239**, 131–138 (2016).
11. Y. Liu, W. Gao, *J. Alloys Compd.*, **629**, 84–91 (2015).
12. Y. Kumar, A. K. Rana, P. Bhojane, M. Pusty, V. Bagwe, *Mater. Res. Express*, **2**, No. 10, 105017 (2015).
13. S. Kanmani, N. Rajamanickam, K. Ramachandran, *Org. Electron.*, **15**, No. 10, 2302–2310 (2014).

14. D. V. Sathish, Ch. Rama Krishna, Ch. Venkata Reddy, T. Raghavendra Rao, P. S. Rao, R. V. S. S. N. Ravikumar, *J. Mol. Struct.*, **1034**, 57–61 (2013).
15. D. V. Sathish, Ch. Rama Krishna, Ch. Venkata Reddy, U. S. Udayachandran Thampy, R. V. S. S. N. Ravikumar, *Phys. Scr.*, **86**, 035708 (2012).
16. P. Shokeen, A. Jain, A. Kapoor, *Opt. Mater.*, **67**, 32–37 (2017).
17. K. Qi, B. Cheng, J. Yu, W. Ho, *J. Alloys Compd.*, **727**, 792–820 (2017).
18. N. Kumaresan, K. Ramamurthi, R. Babu, K. Sethuraman, S. M. Babu, *Appl. Surf. Sci.*, **418**, 138–146 (2017).
19. S. Radhika, J. Thomas, *J. Environ. Chem. Eng.*, **5**, 4239–4250 (2017).
20. S. J. Pearton, F. Ren, *Int. Mater. Rev.*, **59**, 61–83 (2014).
21. Y.-P. Xu Yun, Jin Lu, Ma Xiang-Yang, Yang De-Ren, *Acta Phys. Sin.*, **62**, 84207 (2013).
22. Y.-C. Shen, C.-H. Yang, S.-W. Chen, S.-H. Wu, T.-L. Yang, J.-J. Huang, *Biosens. Bioelectron.*, **54**, 306–310 (2014).
23. M. Hjiri, L. El Mir, S. G. Leonardi, A. Pistone, L. Mavilia, G. Neri, *Sens. Act. B: Chem.*, **196**, 413–420 (2014).
24. V. S. Khomchenko, N. N. Roshchina, L. V. Zavyalova, V. V. Strelchuk, G. S. Svechnikov, N. P. Tatyanenko, V. L. Gromashevskii, O. S. Litvin, E. A. Avramenko, B. A. Snopok, *Tech. Phys.*, **59**, 93–101 (2014).
25. M. Yuste, R. E. Galindo, O. M. Sacristan, I. Minguez-Bacho, R. Sonia, M. Hernandez-Velez, O. Sanchez, *Mater. Res. Express*, **1**, 045028 (2014).
26. W. Zhang, J. Zhao, Z. Liu, Z. Liu, *Appl. Surf. Sci.*, **284**, 49–52 (2013).
27. M. Venkatesan, C. B. Fitzgerald, J. M. D. Coey, *Nature*, **450**, 630 (2004).
28. A. Chakrabarty, C. H. Patterson, *Phys. Rev. B: Condens. Mater. Mater. Phys.*, **84**, 054441 (2011).
29. W. Liu, W. Li, Z. Hu, Z. Tang, X. Tang, *J. Appl. Phys.*, **110**, 013901 (2011).
30. S. Shit, T. Kamilya, P. K. Samanta, *Mater. Lett.*, **118**, 123–125 (2014).
31. M. V. Kuznetsov, Y. G. Morozov, O. V. Belousova, D. Ortega, *Inorg. Mater.*, **50**, 369–378 (2014).
32. S. S. Xiao, L. Zhao, Y. H. Liu, J. S. Lian, *Appl. Surf. Sci.*, **283**, 781–787 (2013).
33. K.S. Babu, A. R. Reddy, K. V. Reddy, *Mater. Res. Bull.*, **49**, 537–543 (2014).
34. G. N. Narayanan, R. S. Ganesh, A. Karthigeyan, *Thin Solid Films*, **598**, 39–45 (2016).
35. K. H. Kim, et al., *Superlattices Microstruct.*, **91**, 188–192 (2016).
36. A. Ghosh, N. G. Deshpande, Y. G. Gudage, R. A. Joshi, A. A. Sagade, D. M. Phase, Ramphal Sharma, *J. Alloys Compd.*, **469**, No. 1-2, 56–60 (2009).
37. T. Akilan, N. Srinivasan, R. Saravanan, *Mater. Sci. Semicond. Proc.*, **30**, 381–387 (2015).
38. H. Morcos, U. Ozgur, *Zinc Oxide: Fundamentals, Materials and Device Technology*, Wiley-VCH (2009).
39. E. N. Budilova, V. A. Nikitenko, S. M. Kokin, *Bull. Russ. Acad. Sci. Phys.*, **79**, 160–164 (2015).
40. V. A. Nikitenko, S. M. Kokin, S. G. Stouhin Anomalies, *J. Appl. Spectrosc.*, **86**, 567–571 (2019).
41. V. A. Nikitenko, *J. Appl. Spectrosc.*, **57**, 783–798 (1992).
42. S. Benramache, et al., *J. Semicond.*, **35**, No. 4, 042001 (2014).
43. S. Deshpande, et al., *Appl. Phys. Lett.*, **87**, No. 13, 133113 (2005).